Letter

Electron beam characterization via quantum coherent electric field imaging

Rob Behary [1,*] Kevin Su [1] Nicolas DeStefano [1] Mykhailo Vorobiov [1] T. Averett [1] Alexandre Camsonne [2] Shukui Zhang [2] Charles T. Fancher [3] Neel Malvania [3] Eugeniy E. Mikhailov [1] Seth Aubin [1] and Irina Novikova [1]

[1]*Department of Physics, William & Mary, 300 Ukrop Way, Williamsburg, Virginia 23185, USA*

[2]*Thomas Jefferson National Accelerator Facility, 12000 Jefferson Avenue, Newport News, Virginia 23606, USA*

[3]*The MITRE Corporation, McLean, Virginia 22102, USA*

(Received 13 May 2025; accepted 19 October 2025; published 25 November 2025)

We demonstrate an all-optical, minimally invasive electron beam (*e*-beam) characterization using Rydberg electrometry. An *e*-beam passes through a localized detector volume containing thermal Rb atoms that are optically excited in a quantum superposition of ground and Rydberg states. The *e*-beam's electric field perturbs atomic coherence and modifies resonance fluorescence in a narrow spectral region near the two-photon optical transition. Imaging Rb fluorescence provides a map of the electric field from the *e*-beam via Rydberg state Stark shifts and allows us to reconstruct the *e*-beam width, centroid position, and current. For an *e*-beam of 20 keV and electron currents of 20–40 μA, we measured the centroid position with an accuracy of $\leqslant 8$ μm and width to within 100 μm, limited by the experimental sensitivity of electric field reconstruction of ∼0.02 V/cm. This method is suitable for a wide range of electron energies and currents, and can be adopted for nuclear and high-energy experiments for minimally invasive real-time diagnostics and profiling of charged particle beams.

DOI: 10.1103/sp9j-ps66

Electron beams are broadly used across science, industry, and medicine for imaging, microscopy, materials processing, welding, lithography, radiation generation, and high-energy particle acceleration, thanks to their ability to deliver precisely controlled, high-energy streams of electrons. As a result, there has been an increasing demand for more robust non-invasive spatial beam property diagnostics. While different approaches and apparatuses exist, optical and imaging methods based on signals such as fluorescence [1,2], synchrotron radiation [3], and x rays generated by moving particles [4] have played an essential role in accelerator research and beam operations. However, each of these beam diagnostics also bears some intrinsic drawbacks, and their applicability is often limited by factors such as sensitivity and system complexity. For example, synchrotron radiation only exists near particle trajectory-bending components [3,5], compton scattering laser wire requires high laser intensity and slow scanning between particle and laser beams [6,7], and the gas-ionization-based two-dimensional gas curtain devices rely on complex mechanical systems and have low sensitivity [8,9]. The work presented here describes a proof-of-principle, sensitive, minimally invasive apparatus capable of measuring multiple charged particle beam parameters, including width, centroid position, and current simultaneously.

We combine the method of laser-induced fluorescence dip, used to observe electric fields in plasmas [10–14] with the technique of electromagnetically induced transparency (EIT) [15–21], which uses quantum coherence for generating narrow linewidths for quantum electrometry. We take advantage of the exceptionally large electron dipole moment of Rydberg states of alkali metal atoms ($n \geqslant 20$) that have already been explored for a wide range of applications. These include SI-traceable electric field standards [22], rf-field receivers [19,21,23], THz-imaging [24–26], magnetic field sensing [27,28], and thermometry of blackbody radiation [29]. Here, we introduce a diagnostic method for an electron beam (*e*-beam) via an all-optical measurement of its effect on the Rydberg states in a dilute rubidium (Rb) vapor. The reconstruction of the electric field, created by the electrons, lets us determine the centroid position, width, and total current of the *e*-beam. Unlike the complimentary technique based on magnetic field reconstruction using nonlinear magneto-polarization rotation [30], the current method offers superior spatial resolution, and in principle allows for three-dimensional reconstruction of the charged particle distribution.

In our experiment, the Rb atoms are excited to a coherent superposition of the ground and Rydberg state using two laser fields: a near-infrared (IR) probe field, resonant with the $5S_{1/2} \rightarrow 5P_{3/2}$ optical transition (wavelength 780 nm), and a 480 nm blue control field that couples the intermediate $5P_{3/2}$ state with the desired Rydberg state (in our experiment $58D_{5/2}$). In this "dark state," the population of the intermediate state diminishes when the sum of the laser frequencies matches the frequency difference between the ground and Rydberg states, and this change can be detected either through increased probe laser transmission (EIT) or reduced IR

*Contact author: rbehary@wm.edu

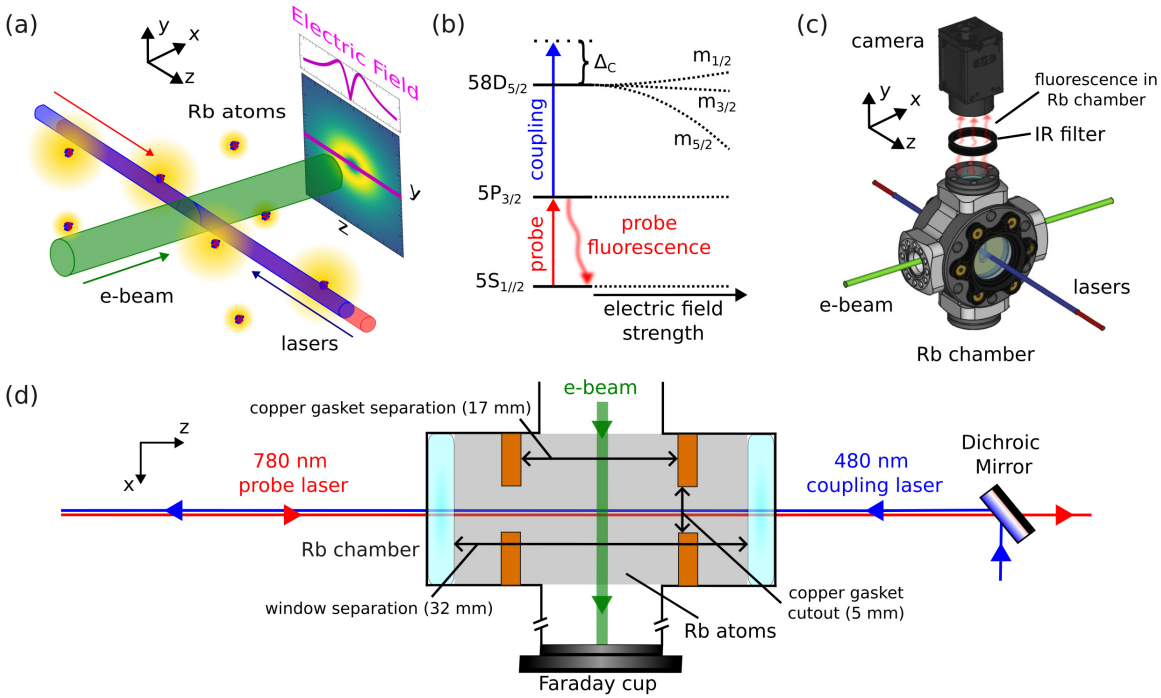

FIG. 1. Overview of experimental design. (a) A charged particle beam produces an electric field and passes through a cloud of Rb atoms shown as a nucleus with a yellow electron cloud. We use lasers to excite these atoms to a Rydberg state (shown as atoms with a larger electron cloud) to probe the electric field. We assume the beam produces a radially symmetric Gaussian electric field distribution described by Eq. (3). (b) Energy level diagram for Rydberg EIT. In the presence of an electric field, the $|m_j|$ sublevels of the Rydberg state will shift differently based on the strength of electric field. (c) Experimental setup to capture the probe laser fluorescence in the Rb chamber with a camera. (d) Cross section of Rb chamber on our beam line for electric field detection (not to scale). Relevant distances are marked. The Faraday cup's position is shown representatively, but is in fact located 20 cm away from Rb chamber.

fluorescence [31,32] in a relatively narrow frequency range around the two-photon resonance (around a few tens of MHz or less) [16]. Such an arrangement allows for relatively simple and sensitive detection of Rydberg state frequency shifts caused by external electric and magnetic fields. To maximize the interaction volume and, more importantly, to minimize the two-photon Doppler broadening [18], the two optical fields are typically counterpropagating. Monitoring the probe laser transmission has been done to spatially map electric fields in the past [33,34], but we use a recently demonstrated coherent fluorescence-based imaging technique [28,35] to map the electric field produced by an *e*-beam. By recording and analyzing the spatial variation of IR fluorescence in the Rydberg EIT configuration, we map spatial variations of the dc electric field along the probe laser beam path.

The experimental setup and general detection principle for the *e*-beam diagnostics are shown in Fig. 1. A collimated beam of 20 keV electrons passes through an area filled with a dilute Rb vapor. The Rb density of $\approx 1.6 \times 10^{11}$ atoms/cm^3 is produced using an ampule of metallic Rb placed in the heated vacuum chamber (55 °C partial pressure $\simeq 5 \times 10^{-6}$ Torr). Figure 1(a) also shows a radially symmetric electric field distribution, produced by an *e*-beam with a Gaussian transverse profile. Two counter-propagating laser beams, perpendicular to the *e*-beam, are used to excite Rb atoms to the 58D Rydberg state. The electric field lifts the degeneracy of this state, producing quadratic dc-Stark shifts for each of the $|m_j|$ sublevels, as shown in Fig. 1(b). Approximate shifts to the Rydberg sublevels are described by

$$\Delta f_{|m_j|}(E) = -\tfrac{1}{2}\alpha_{|m_j|}E^2/h, \tag{1}$$

where h is Planck's constant, $\alpha_{|m_j|}$ is the polarizability of the different $|m_j|$ sublevels of the Rydberg state, and E is the magnitude of the electric field [19,22,28,35]. A more accurate description of these shifts is interpolated from a numerically solved Stark map generated by the alkali Rydberg calculator (ARC) [36].

The effect of dc Stark shifts on the EIT resonance at different points along the laser beam is monitored using a camera. The camera captures the probe laser fluorescence in the Rb chamber Fig. 1(c). For these measurements, we need to capture the variation in $5P_{3/2}$ state population as a function of the coupling laser frequency at each spatial point along the probe laser fluorescence. To do that, the camera collects images at a fixed frame rate with 60 ms exposure time for 600 frames while the coupling laser sweeps across the 58D Rydberg state for 300 s. This way, we are able to record the fluorescence spectrum for each image pixel, providing localized information of electric field. We use the known frequency separation of the $58D_{5/2}$ and $58D_{3/2}$ Rydberg states [36] to calibrate the frequency axis. For these measurements, both laser fields were collimated to a similar beam size [0.33 mm full width at half maximum (FWHM)] and have the same linear polarization along the y axis. Laser beam sizes are much narrower than the size of the *e*-beam measured to have an FWHM of 1.07 ± 0.06 mm. The 780 nm probe laser has

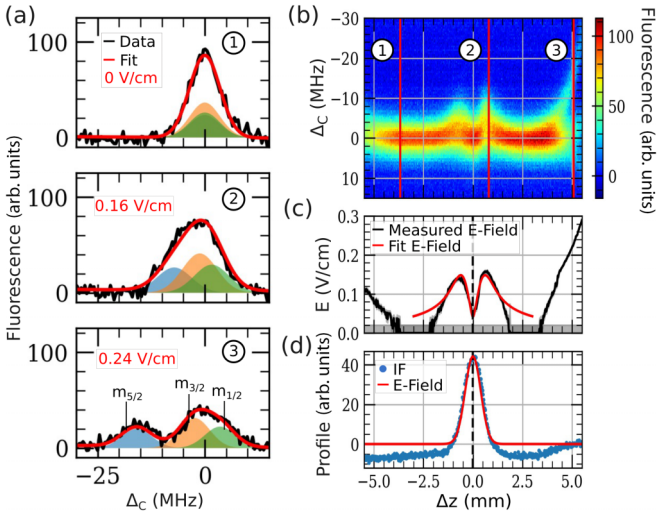

FIG. 2. Demonstration of fluorescence-based measurements of the electric field of an *e*-beam. (a) The EIT spectra that constitute the heat map in panel (b). The spectra are fit with Eq. (2) to determine the electric field value shown as the shaded regions in each plot. (b) The measured spectra of the $58D_{5/2}$ Rydberg EIT peak for each position along the laser beam fluorescence. The numbers correspond to the shown single spectra in panel (a). (c) The reconstructed electric field value along the Rb chamber. The measured field is fit with a function described by Eq. (3). The minimum detectable field is shown as a gray strip along the bottom of the plot, and error bars on the fit are also shown in gray. (d) *e*-beam profile. IF shows a detection method to verify where the *e*-beam is inside the Rb chamber, and the reconstructed profile from the *E*-field measurement is plotted on top of the IF profile.

a power of 5 μW, and the maximum power of the 480 nm coupling laser is 70 mW. We used a 50 mm lens to image the plane of the laser fluorescence in the Rb chamber onto the camera. An IR filter in front of the lens eliminates background light and increases the signal-to- noise ratio (SNR) for the probe laser fluorescence.

A more detailed view of the experimental arrangements in Fig. 1(d) shows the location of grounded copper gaskets whose role is to attenuate possible electric charge buildup on the fused silica chamber windows from scattered electrons or photoelectrons produced by the blue laser [33,35]. The *e*-beam itself is a commercial tungsten hairpin thermionic electron source with an energy spread of 0.8–1.2 eV. The beam energy is fixed at 20 keV and current is varied from 0 to 40 μA monitored by a Faraday cup and an integrated parametric current transformer placed along the beamline.

We cannot measure the current in the Rb chamber, but we can obtain *in situ* information about the *e*-beam position and size by measuring beam impact fluorescence (IF)—the incoherent electron impact-induced fluorescence in Rb [1,30,37]. In this case, all the lasers are blocked, and the Rb fluorescence caused solely by the *e*-beam is recorded with a 10 s exposure time using the same imaging system. IF offers a secondary *in situ* measurement of the *e*-beam position and size to compare with the Rydberg measurements.

Figure 2 shows an example of the recorded fluorescence spectra and resulting *e*-beam profile analysis. Figure 2(a) shows three samples of the EIT fluorescence spectra for different positions along the laser beam path [Fig. 2(b)]: (1) at the region of minimal electric field; (2) at the edge of the *e*-beam where its electric field is the highest; and (3) near the surface of the copper blank gasket where residual charging produces a relatively strong electric field. To extract the value of the electric field at each point, we follow the procedure similar to the previously published work [28,35], where the total EIT fluorescence spectra $\mathcal{F}$ is modeled as a combination of three Gaussian resonances:

$$\mathcal{F} = A\sum_{|m_j|} w_{|m_j|}\exp\left[\frac{-[\Delta_C - \Delta f_{|m_j|}(E)]^2}{2\gamma_{\text{EIT}}^2}\right]. \quad (2)$$

Here, $w_{|m_j|}$ are amplitudes for each $|m_j|$ level of the Rydberg state empirically set and constant for all fits, Δ_C is the coupling laser frequency detuning, γ_{EIT} is the linewidth of the EIT resonance set constant for all fits, and $\Delta f_{|m_j|}(E)$ is the frequency shift of the Rydberg energy level described by the Stark map from ARC [28,35,36]. While the EIT lineshape should be Lorentzian, due to broadening of the resonances Gaussian curves fit the data well. In this fit, the only free parameters are the total amplitude of the EIT profile, A, and the value of electric field magnitude E [38].

The reconstructed electric field distribution is shown in Fig. 2(c). In the center, one can clearly see the characteristic two-lobed feature, expected when the laser beams go through the center of the *e*-beam, as shown in Fig. 1(a). The position and width of this feature match well with the IF signal as shown in Fig. 2(d). The background electric field near the edges is not directly related to the *e*-beam, but caused by residual charging of the cell windows and walls. The smallest measurable electric field value is limited by the smallest detectable shift. We can estimate it as $\simeq \gamma_{\text{EIT}}/(\text{SNR}\sqrt{n}) = 0.1$ MHz [39,40], where SNR ≈ 20 is the signal-to-noise ratio (defined as a ratio between EIT resonance amplitude and the standard deviation in each frequency bin) and $n \approx 90$ is the number of data points within the linewidth of a recorded resonance. This corresponds to a minimum detectable electric field of $E_{\text{min}} \approx 0.02$ V/cm, which matches our more thorough statistical analysis with simulated data of similar SNR. The precision of the reconstructed electric field value improves for higher electric field, because of nonlinear Stark shift dependence on applied field, and at field values around 0.1 V/cm the precision is <0.01 V/cm. We note that to achieve this precision, it is crucial to link resonance shifts via the Stark splitting model (rather than fitting them independently) and to keep fixed widths and amplitudes of contributing resonances.

To extract the *e*-beam parameters, we fit the reconstructed curve with an analytical expression for the electric field produced by an electron beam with a Gaussian distribution:

$$E_{e\text{-beam}} = \frac{I}{2\pi\epsilon_0 v_e}\frac{1}{r}\left(1 - e^{-\frac{r^2}{\sigma^2}}\right). \quad (3)$$

Here, σ is related to the width of the *e*-beam by FWHM $= 2\sigma\sqrt{\ln(2)}$, ϵ_0 is the permittivity of free space, $r = \sqrt{(\Delta z - z_0)^2 + (\Delta y - y_0)^2}$ is the radial position away from the *e*-beam center, z_0 is its displacement along the z direction, I is the *e*-beam current, and v_e is the speed of the electron, proportional to the square root of the beam energy. The fit also

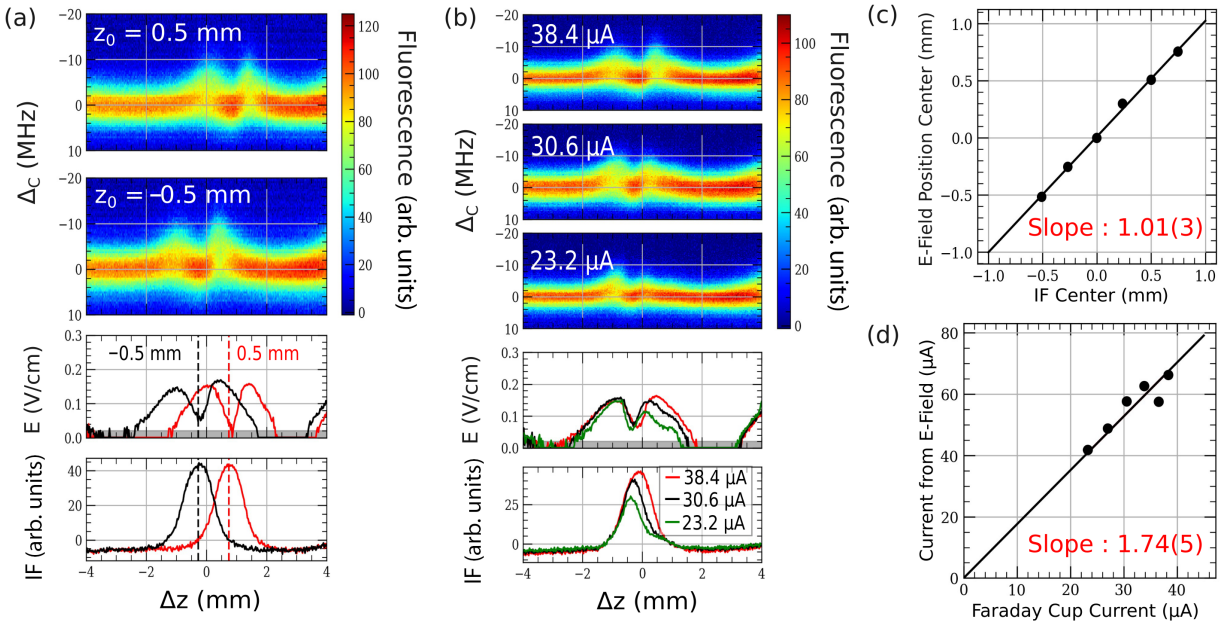

FIG. 3. *e*-beam diagnostics for position and current. Panels (a) and (b) are the same style of plots shown in Figs. 2(b)–2(d). (a) Heat maps for two different *e*-beam positions in the cell. The dashed lines in the plots show the beam center. (b) Plots of heat maps for increasing *e*-beam current. Current values recorded from the Faraday cup. (c) Diagnostic of *e*-beam position in the Rb chamber. Error bars on the plot are derived from the uncertainty of the fit and smaller than the points on the graph. (d) Fit of recovered Rydberg current vs Faraday cup current. Error bars on the plot are derived from uncertainty of the fit and smaller than the points on the graph.

accounts for the finite width of the laser beam and the y deflection from the center of the *e*-beam. The free parameters in this fit are the *e*-beam width σ, *e*-beam current I, and the z_0 and y_0 displacement of the electron and laser beams, respectively. We only fit the region of the reconstructed electric field, where $|\Delta z| \leqslant 3$ mm because it avoids the large parasitic background field, and we found that varying this range has little effect on the reconstructed width, current and centroid position.

The reconstructed *e*-beam cross section is plotted on top of the IF measurement in Fig. 2(d), showing excellent agreement between the two measurement methods. The *e*-beam FWHM is measured to be 1.07 ± 0.06 mm with the IF method and 1.1 ± 0.1 mm with the Rydberg electric field reconstruction method. The value of the width is measured from repeated measurements with a fixed Faraday cup current of 35 μA.

Further diagnostics of the *e*-beam position and current are shown in Fig. 3. For these measurements, we either moved the *e*-beam [Fig. 3(a)] or changed its current [Fig. 3(b)] and tracked the variations in the reconstructed electric field distribution. For example, if the beam position changes, the two lobes shift by the corresponding amount. To verify the accuracy of our method, we fit the reconstructed electric field with a functional form, as described above. Figure 3(c) shows excellent agreement between the reconstructed beam position with that measured using the IF method. The shown uncertainties for the Rydberg EIT methods are from the error of the fit parameters, and the centroid position is known within 8 μm.

Changing the emission current seems to also slightly deform and shift the *e*-beam due to electron repulsion or focusing effects that we see in both electric field reconstruction [Fig. 3(b)] and IF measurements. Both profiles show an asymmetry that may be due to the background field present within the Rb chamber visible near the edges. Figure 3(d) shows a clear linear correlation between the recorded Faraday cup current and the current values reconstructed from the electric field. The reconstructed current values are about twice larger than the measured Faraday cup current, possibly due to the *e*-beam clipping somewhere in the beamline before the Faraday cup. Further verification will require accurate *in situ* *e*-beam current measurements using, e.g., a co-located harp scanner. Since our current approach is only sensitive to the absolute value of the electric field, our current fit model does not take into account the direction of the electric field, and its influence on the shifts and transition amplitudes of the different $|m_j|$ levels of the Rydberg state. We also note that magnetic fields can distort the EIT resonance [27], but we have shielding for ambient magnetic fields and the magnetic field produced by the *e*-beam is small compared to what is needed to modify the resonance [30]. In addition, presence of the background electric field can produce additional systematic error in beam reconstruction due to its unknown direction. More accurate current measurements will require improvement of the Rb vapor chamber design to further reduce the parasitic charging.

In conclusion, we apply Rydberg fluorescence-based detection to measure spatially varying dc electric fields produced by an *e*-beam and to reconstruct the center-of-mass beam position to within 8 μm, determine the beam width to within 100 μm, and measure the beam current in a simultaneous measurement. We expect this technique to be useful for diagnostics of charged particle beams of any energy, and for diagnostics of charged particles in general, such as in low-density plasmas [10–14,41,42]. Further diagnostics such as full beam cross-sectional profiling can be achieved using sheet laser beams [28,43], especially if the full electric field vector is reconstructed [44,45]. The detection speed can be

improved by using a faster higher dynamic range camera or an array of Rydberg atoms to study the temporal dynamics of electron beams [46]. The method can be extended to use the transmission of the probe laser by using crossed laser beams [47] or a three-photon "star" configuration [48], but at the expense of reduced spectral resolution and lower signal-to-noise.

The authors thank Saeed Pegahan and Ziqi Niu for help with experiments, and Christopher L. Holloway's group at NIST and Sergei Nagaitsev for helpful conversations. This work was supported by U.S. DOE Contracts No. DE-SC0024621 and No. DE-AC05-06OR23177, NSF Award No. PHYS2326736, and Jefferson Lab LDRD program. Approved for Public Release; Distribution Unlimited. Public Release Case Number 25-1266.

Data availability. The data that support the findings of this article are not publicly available upon publication because it is not technically feasible and/or the cost of preparing, depositing, and hosting the data would be prohibitive within the terms of this research project. The data are available from the authors upon reasonable request.

[1] A. Salehilashkajani, H. D. Zhang, M. Ady, N. Chritin, P. Forck, J. Glutting, O. R. Jones, R. Kersevan, N. Kumar, T. Lefevre, T. Marriott-Dodington, S. Mazzoni, I. Papazoglou, A. Rossi, G. Schneider, O. Sedlacek, S. Udrea, R. Veness, and C. P. Welsch, A gas curtain beam profile monitor using beam induced fluorescence for high intensity charged particle beams, Appl. Phys. Lett. **120**, 174101 (2022).

[2] D. P. Sandoval, R. C. Garcia, J. D. Gilpatrick, M. A. Shinas, R. Wright, V. Yuan, and M. E. Zander, Fluorescence-based video profile beam diagnostics: Theory and experience, AIP Conf. Proc. **319**, 273 (1994).

[3] A. Hofmann, Electron and proton beam diagnostics with synchrotron radiation, IEEE Trans. Nucl. Sci. **28**, 2131 (1981).

[4] D. W. Rule, Transition radiation diagnostics for intense charged particle beams, Nucl. Instrum. Methods Phys. Res., Sect. B **24–25**, 901 (1987).

[5] L. Ponce, R. Jung, and F. Meot, LHC proton beam diagnostics using synchrotron radiation, Technical Report, 2004.

[6] K. Chouffani, F. Harmon, D. Wells, J. Jones, and G. Lancaster, Laser-compton scattering as a tool for electron beam diagnostics, Laser Part. Beams **24**, 411 (2006).

[7] G. Blair, Laser based beam diagnostics, EUROTeV-Report-2008-027 EUROTeV-Report-2008-027, 2008.

[8] V. Tzoganis, H. D. Zhang, A. Jeff, and C. P. Welsch, Design and first operation of a supersonic gas jet based beam profile monitor, Phys. Rev. Accel. Beams **20**, 062801 (2017).

[9] C. C. Sequeiro, M. Ady, G. Bregliozzi, N. Chatzigeorgiou, A.R. Churchman, R. Kersevan, T. Lefevre, S. Mazzoni, G. Pigny, O. Stringer, A. Webber-Date, C.P. Welsch, H. Zhang, P. Forck, S. Udrea, A. Rossi, M. Sameed, G. Schneider, O. Sedlacek, K. Sidorowski *et al.*, Beam gas curtain monitor: Vacuum studies for LHC integration and operation, Phys. Rev. Accel. Beams **27**, 043201 (2024).

[10] U. Czarnetzki, D. Luggenhölscher, and H. F. Döbele, Sensitive electric field measurement by fluorescence-dip spectroscopy of Rydberg states of atomic hydrogen, Phys. Rev. Lett. **81**, 4592 (1998).

[11] E. Wagenaars, G. M. W. Kroesen, and M. D. Bowden, Investigations of Stark effects in xenon Rydberg states by laser-induced fluorescence-dip spectroscopy, Phys. Rev. A **74**, 033409 (2006).

[12] E. V. Barnat and G. A. Hebner, Electric fields in a sheath near a metal–dielectric interface, Appl. Phys. Lett. **85**, 3393 (2004).

[13] U. Czarnetzki, D. Luggenhölscher, and H. Döbele, Space and time resolved electric field measurements inhelium and hydrogen RF-discharges, Plasma Sources Sci. Technol. **8**, 230 (1999).

[14] W. An, Z. Wang, A. Weisenburger, and G. Mueller, Laser-induced fluorescence-dip spectroscopy of Rydberg states of xenon for electric field measurement in plasma, Rev. Sci. Instrum. **93**, 023503 (2022).

[15] M. O. Scully and M. S. Zubairy, *Quantum Optics* (Cambridge University Press, Cambridge, UK, 2001).

[16] A. K. Mohapatra, T. R. Jackson, and C. S. Adams, Coherent optical detection of highly excited Rydberg states using electromagnetically induced transparency, Phys. Rev. Lett. **98**, 113003 (2007).

[17] T. F. Gallagher, *Rydberg Atoms*, Cambridge Monographs on Atomic, Molecular and Chemical Physics (Cambridge University Press, Cambridge, UK, 1994).

[18] R. Finkelstein, S. Bali, O. Firstenberg, and I. Novikova, A practical guide to electromagnetically induced transparency in atomic vapor, New J. Phys. **25**, 035001 (2023).

[19] N. Schlossberger, N. Prajapati, S. Berweger, A. P. Rotunno, A. B. Artusio-Glimpse, M. T. Simons, A. A. Sheikh, E. B. Norrgard, S. P. Eckel, and C. L. Holloway, Rydberg states of alkali atoms in atomic vapour as SI-traceable field probes and communications receivers, Nat. Rev. Phys. **6**, 606 (2024).

[20] M. T. Simons, A. B. Artusio-Glimpse, A. K. Robinson, N. Prajapati, and C. L. Holloway, Rydberg atom-based sensors for radio-frequency electric field metrology, sensing, and communication, Meas.: Sens. **18**, 100273 (2021).

[21] C. T. Fancher, D. R. Scherer, M. C. S. John, and B. L. S. Marlow, Rydberg atom electric field sensors for communications and sensing, IEEE Trans. Quantum Eng. **2**, 1 (2021).

[22] C. L. Holloway, M. T. Simons, J. A. Gordon, A. Dienstfrey, D. A. Anderson, and G. Raithel, Electric field metrology for SI traceability: Systematic measurement uncertainties in electromagnetically induced transparency in atomic vapor, J. Appl. Phys. **121**, 233106 (2017).

[23] P. K. Elgee, J. C. Hill, K.-J. E. LeBlanc, G. D. Ko, P. D. Kunz, D. H. Meyer, and K. C. Cox, Satellite radio detection via dual-microwave Rydberg spectroscopy, Appl. Phys. Lett. **123**, 084001 (2023).

[24] C. G. Wade, N. Šibalić, N. R. De Melo, J. M. Kondo, C. S. Adams, and K. J. Weatherill, Real-time near-field terahertz imaging with atomic optical fluorescence, Nat. Photonics **11**, 40 (2017).

[25] L. A. Downes, L. Torralbo-Campo, and K. J. Weatherill, A practical guide to terahertz imaging using thermal atomic vapour, New J. Phys. **25**, 035002 (2023).

[26] L. A. Downes, A. R. MacKellar, D. J. Whiting, C. Bourgenot, C. S. Adams, and K. J. Weatherill, Full-field terahertz imaging

at kilohertz frame rates using atomic vapor, Phys. Rev. X **10**, 011027 (2020).

[27] N. Schlossberger, A. P. Rotunno, A. B. Artusio-Glimpse, N. Prajapati, S. Berweger, D. Shylla, M. T. Simons, and C. L. Holloway, Zeeman-resolved Autler-Townes splitting in Rydberg atoms with tunable resonances and a single transition dipole moment, Phys. Rev. A **109**, L021702 (2024).

[28] N. Schlossberger, T. McDonald, K. Su, R. Talashila, R. Behary, C. L. Patrick, D. Hammerland, E. E. Mikhailov, S. Aubin, I. Novikova, C. L. Holloway, and N. Prajapati, Two-dimensional imaging of electromagnetic fields via light-sheet fluorescence imaging with Rydberg atoms, Opt. Lett. **50**, 7312 (2025).

[29] N. Schlossberger, A. P. Rotunno, S. P. Eckel, E. B. Norrgard, D. Manchaiah, N. Prajapati, A. B. Artusio-Glimpse, S. Berweger, M. T. Simons, D. Shylla, W. J. Watterson, C. Patrick, A. Meraki, R. Talashila, A. Younes, D. S. La Mantia, and C. L. Holloway, Primary quantum thermometry of mm-wave blackbody radiation via induced state transfer in Rydberg states of cold atoms, Phys. Rev. Res. **7**, L012020 (2025).

[30] N. DeStefano, S. Pegahan, A. Ramaswamy, S. Aubin, T. Averett, A. Camsonne, S. Malinovskaya, E. E. Mikhailov, G. Park, S. Zhang, and I. Novikova, Electron beam characterization via quantum coherent optical magnetometry, Appl. Phys. Lett. **125**, 264001 (2024).

[31] J. Keaveney, A. Sargsyan, D. Sarkisyan, A. Papoyan, and C. S. Adams, Active narrowband filtering, line narrowing and gain using ladder electromagnetically induced transparency in an optically thick atomic vapour, J. Phys. B: At., Mol. Opt. Phys. **47**, 075002 (2014).

[32] L. Ma, Electromagnetic field sensing with Rydberg Atoms in vapor cells, Ph.D. thesis, University of Michigan, 2021.

[33] L. Ma, E. Paradis, and G. Raithel, Dc electric fields in electrode-free glass vapor cell by photoillumination, Opt. Express **28**, 3676 (2020).

[34] Y.-Y. Jau and T. Carter, Vapor-cell-based atomic electrometry for detection frequencies below 1 kHz, Phys. Rev. Appl. **13**, 054034 (2020).

[35] L. Patrick, N. Schlossberger, D. F. Hammerland, N. Prajapati, T. McDonald, S. Berweger, R. Talashila, A. B. Artusio-Glimpse, and C. L. Holloway, Imaging of induced surface charge distribution effects in glass vapor cells used for Rydberg atom-based sensors, AVS Quantum Sci. **7**, 024401 (2025).

[36] N. Šibalić, J. Pritchard, C. Adams, and K. Weatherill, Arc: An open-source library for calculating properties of alkali Rydberg atoms, Comput. Phys. Commun. **220**, 319 (2017).

[37] M. Ugoletti, C. Ballage, T. Minea, G. Serianni, O. Vasilovici, and M. Agostini, Visible cameras as a tool to study electron beam shape, Rev. Sci. Instrum. **96**, 023705 (2025).

[38] While the relative orientation of the electric field laser wave vector and polarization certainly changes the relative amplitude of various m_J resonances, in the reported experiments, we used the configuration in which the resonance amplitudes were relatively insensitive to changes in the e-field direction, so it was possible to not include their variations in the fit. In the future, we hope to use the amplitude variations to measure the electric field direction.

[39] A. G. Marshall and F. R. Verdun, *Fourier Transforms in NMR, Optical, and Mass Spectrometry: A User's Handbook* (Elsevier, Amsterdam, The Netherlands, 1990).

[40] E. E. Mikhailov, I. Novikova, M. D. Havey, and F. A. Narducci, Magnetic field imaging with atomic Rb vapor, Opt. Lett. **34**, 3529 (2009).

[41] S. Mordjick, I. Novikova, E. Mikhailov, and S. Aubin, Optical Quantum Sensing Diagnostic Development for Non-Invasive Measurements of Electric and Magnetic Fields in Plasmas, DOE BRN Workshop on Measurement Innovation, Washington, D.C., Jan. 9, 2024, https://web.cvent.com/event/c6850a60-69dc-489d-9345-1d47a5d704d2/summary.

[42] D. A. Anderson, G. Raithel, M. Simons, and C. L. Holloway, Quantum-optical spectroscopy for plasma electric field measurements and diagnostics, arXiv:1712.08717.

[43] N. Schlossberger, R. Talashila, N. Prajapati, and C. L. Holloway, Angle-of-arrival detection of radio-frequency waves via Rydberg-atom fluorescence imaging of standing waves in a glass vapor cell, Phys. Rev. Appl. **24**, 024056 (2025).

[44] P. K. Elgee, K. C. Cox, J. C. Hill, P. D. Kunz, and D. H. Meyer, Complete three-dimensional vector polarimetry with a Rydberg-atom Rf electrometer, Phys. Rev. Appl. **22**, 064012 (2024).

[45] J. A. Sedlacek, A. Schwettmann, H. Kübler, and J. P. Shaffer, Atom-based vector microwave electrometry using rubidium Rydberg atoms in a vapor cell, Phys. Rev. Lett. **111**, 063001 (2013).

[46] A. Kawasaki, Tracking a nonrelativistic charge with an array of Rydberg atoms, Phys. Rev. Res. **5**, 043178 (2023).

[47] K. Su, R. Behary, S. Aubin, E. E. Mikhailov, and I. Novikova, Two-photon Rydberg EIT resonances in non-collinear beam configurations, J. Opt. Soc. Am. B **42**, 757 (2025).

[48] P. B. Weichman, Doppler sensitivity and resonant tuning of Rydberg atom-based antennas, J. Phys. B: At., Mol. Opt. Phys. **57**, 165501 (2024).